Journal of Hydrology 562 (2018) 155–167

Contents lists available at ScienceDirect

Journal of Hydrology

journal homepage: www.elsevier.com/locate/jhydrol

Research papers

Seasonal and diurnal evaporation from a deep hypersaline lake: The Dead Sea as a case study

I. Hamdani[a,b], S. Assouline[c], J. Tanny[c,d], I.M. Lensky[e], I. Gertman[f], Z. Mor[a,b], N.G. Lensky[a,*]

[a] Geological Survey of Israel, Jerusalem, Israel
[b] Institute of Earth Sciences, The Hebrew University of Jerusalem, Israel
[c] Institute of Soil, Water and Environmental Sciences, Agricultural Research Organization, Volcani Center, Rishon LeZion, Israel
[d] HIT – Holon Institute of Technology, Holon, Israel
[e] Department of Geography and Environment, Bar Ilan University, Ramat-Gan, Israel
[f] Israel Oceanographic and Limnological Research, Haifa, Israel

ARTICLE INFO

This manuscript was handled by Marco Borga, Editor-in-Chief, with the assistance of Di Long, Associate Editor

Keywords:
Eddy covariance
Net radiation
Wind speed
Vapor pressure difference
Water activity
Thermal stability

ABSTRACT

Evaporation plays a major role in lake systems, as it affects the water, energy and solutes budgets. Water salinity reduces evaporation, and as a result affects the energy budget of the lake, including stored heat. In this study, we explore the seasonal and diurnal variations of evaporation and other energy fluxes over the Dead Sea, the deepest and saltiest hypersaline lake on Earth. We present two consecutive years observations using Eddy Covariance system, meteorological stations and a buoy station measuring the water column properties. These observations reveal the effects of synoptic and mesoscale atmospheric circulation on lake evaporation. The seasonal cycle of evaporation is characterized by two peaks. The summer evaporation peak is related to high radiation inputs. The winter peak stem from the high heat storage of the deep lake, with evaporation driven by high vapor pressure demand, combined with synoptic scale wind systems and thermal instability. In summer, the synoptic circulation is stable, providing a weak background wind velocity (Persian trough), hence, the dominant diurnal wind pattern is induced by the Mediterranean Sea Breeze (mesoscale circulation). The two years of eddy covariance measurements in the hypersaline Dead Sea, located in a hyperarid region, revealed annual evaporation rate of $1.13 \pm 0.13\,\mathrm{m\,yr^{-1}}$. We explored several evaporation models versus the directly measured evaporation, and found that the most reliable is a mass transfer model, that was calibrated here for the Dead Sea.

1. Introduction

1.1. Evaporation from saline lakes

Evaporation is the connecting link between the water, salt and energy budgets of lakes: water molecules consume energy to change phase from liquid to vapor while leaving the dissolved ions in the remaining water (Brutsaert, 1982; Assouline, 1993; Lensky et al., 2005). Evaporation is driven by the vapor pressure difference (Δe) between the water surface (e_s) and the overlying air (e_a) (Brutsaert, 1982; Dalton, 1802). Δe is a function of water surface and air temperatures and relative humidity (T_s, T_a, RH), and in saline water, it is also a function of water activity (β):

$$\Delta e = \beta \cdot e_{sat}(T_s) - RH \cdot e_{sat}(T_a) \quad (1)$$

where e_{sat} is the saturation vapor pressure, (Eq. (2)); e_{sat} is multiplied by β and RH, to obtain vapor pressure of brine surface and overlying air (e_s and e_a, respectively). As water salinity rises, the water activity decreases (Salhotra et al., 1985). From Eq. (1) it appears that, under given conditions, the evaporation rate from saline water will be lower compared to that from fresh water following the reduction of Δe (Mor et al., 2018). In addition to the driving force given by Eq. (1), evaporation is controlled by wind speed and thermal stability of the overlying boundary layer, i.e. the vapor transport agents which affect the resistance in the process. The depth of the water body has a great influence on evaporation, since the heat stored in the water column dictates the surface water temperature, and hereby affects Δe and thermal stability; a deep lake will have a slower response to varying atmospheric conditions than a shallow pond due to its higher thermal inertia, which provides heat flux for evaporation over longer times, in the diurnal and seasonal cycles. Thus, evaporation from deep lakes is expected to be influenced by both the properties and dynamics of the water body, including the water thermal stratification and the surface water salinity, and by the properties and dynamics of the overlying atmospheric

* Corresponding author.
E-mail address: nadavl@gsi.gov.il (N.G. Lensky).

https://doi.org/10.1016/j.jhydrol.2018.04.057
Received 25 December 2017; Received in revised form 20 April 2018; Accepted 25 April 2018
Available online 27 April 2018

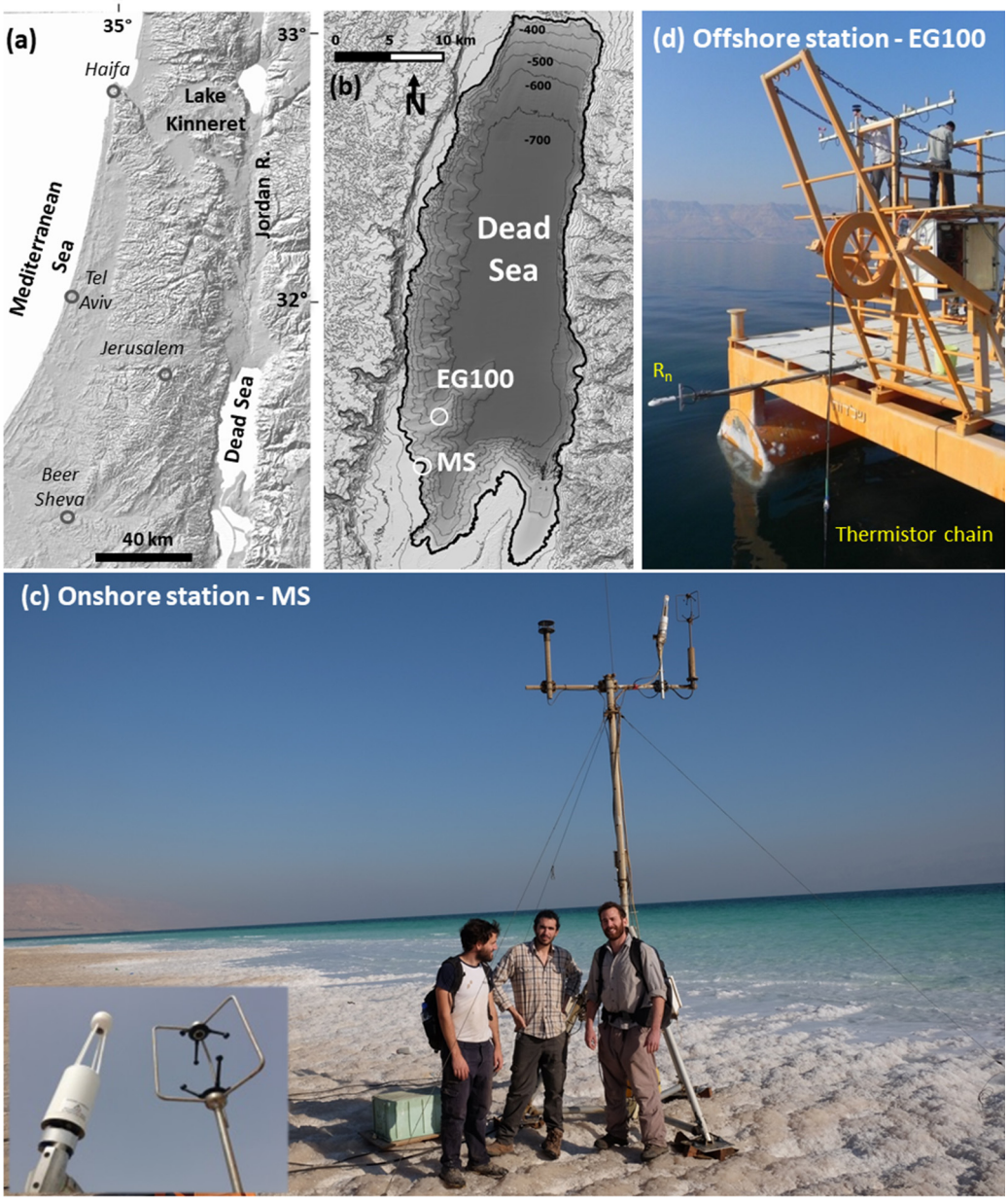

Fig. 1. Sites and measurement systems: (a) Map of the Dead Sea vicinity (DEM hillshade), (b) Location of MS and EG100 stations. (c) The onshore station – MS – an eddy covariance tower with a meteorological station (insert – the eddy covariance sensors). Note the white salt (halite) ground cover due to exposure of the lake floor. (d) The offshore station – EG100 – a meteorological buoy with a thermistor chain within the water column and a net radiometer.

boundary layer.

The Dead Sea is the saltiest deep lake on earth, providing a rare opportunity to explore diurnal and seasonal evaporation and surface heat fluxes from a deep hypersaline lake located in a hyper-arid region, and the lake's response to the forcing of the atmospheric conditions.

1.2. Evaporation from the Dead Sea

The Dead Sea (Fig. 1) is a hypersaline (salinity $> 277\ g\ kg^{-1}$) terminal lake located at the lowest subaerial surface on earth (-431 m amsl, at observation period), with the highest surface water density ($> 1.24\ gr\ cm^{-3}$, Arnon et al., 2016; Hect and Gertman, 2003; Sirota et al., 2016) among earths deep lakes (depth ~ 290 m and surface area of $\sim (630\ km^2$, Sade et al., 2014). It is a holomictic lake; vertically mixed during winter and stratified during the warm summer (Anati, 1997; Arnon et al., 2016; Hect and Gertman, 2003; Nehorai et al., 2009; R. Nehorai et al., 2013a, 2013b; Sirota et al., 2016). During the past decades, the Dead Sea is experiencing a dramatic level decline, $> 1\ m\ yr^{-1}$, due to the diversion of water resources from this terminal lake, mainly from the Jordan River drainage basin (Lensky and Dente, 2017). As a result, the salinity increased until reaching the saturation of halite, and since then (Steinhorn, 1983; Steinhorn and Assaf, 1980) halite is continuously deposited in the lake floor at a rate of $\sim 0.1\ m\ yr^{-1}$ (Lensky et al., 2005; Stiller et al., 1997).

The 'Persian trough' is the dominant synoptic scale atmospheric circulation pattern prevailing during the summer (mid-May to mid-September) over the Eastern Mediterranean, including the Dead Sea region. It is an extension of a low-pressure system over the Persian Gulf reaching the Eastern Mediterranean region (Lensky and Dayan, 2015). The 'Persian trough' provides weak synoptic scale forcing, favorable for mesoscale flows, like the Mediterranean Sea Breeze, generated by the daytime differential surface heating between land and sea (Lensky and Dayan, 2012; Levy et al., 2010). In all other seasons, the synoptic scale circulation is dominant, varying on scale of few days.

Proper characterization of evaporation and other energy fluxes over the Dead Sea across various time scales are very important for understanding the dynamics of hypersaline deep water bodies, including the water and heat budgets, and the salt deposit spatio-temporal dynamics (Sirota et al., 2016; Sirota et al., 2017).

Evaporation estimations from water bodies can be made by direct or indirect methods. The eddy covariance technique is a direct method, that under certain limitations considered to be the most accurate and reliable technique for evaporation measurements (Itier and Brunet, 1996); however it requires expensive instruments and highly demanding data analysis. The indirect methods for evaporation estimation are more commonly used and include mass (water and salt) balance, energy budgets and mass transfer models (Brutsaert, 2005); however these could be associated with relatively large uncertainties (Assouline, 1993). The water balance approach should be quite straightforward to estimate evaporation in the Dead Sea since it is a terminal lake, meaning that knowing the changes in the volume of the lake and the inflows, evaporation can be calculated as the residual flux. However, whereas the lake level and bathymetry are measured with minor uncertainties ($< 1\%$ on an annual basis), the inflows discharge, pumping of the potash industries and the discharged end brine are not well monitored, leading to uncertain evaporation estimates. Following the approach applied in Lake Kinneret (Assouline, 1993), Lensky et al. (2005) proposed a water, energy and salt budgets scheme for the Dead Sea, to reduce the large uncertainties associated with the balance approach in estimating evaporation. The estimates of mean annual evaporation from the Dead Sea based on these indirect approaches range from $\sim 1\,m\,yr^{-1}$ (Stanhill, 1994) to $\sim 2\,m\,yr^{-1}$ (Salameh and El-Naser, 1999). Direct evaporation measurements can be used for comparison with evaporation models, as was done in freshwater surfaces (Assouline and Mahrer, 1993; Stannard and Rosenberry, 1991; Tanny et al., 2008, 2011).

Direct measurements of evaporation and sensible heat flux were conducted by means of eddy covariance, over lakes, reservoirs and seas, with variable salinity from freshwater up to the salinity of ocean water (Allen and Tasumi, 2005; Assouline et al., 2008; Liu et al., 2012, 2009; MacKellar and McGowan, 2010; McGowan and Sturman, 2010). Recently, eddy covariance evaporation measurements were conducted in the Dead Sea. Lensky et al. (2018) showed that during summer evaporation is characterized by a diurnal double peak, one peak related to radiative heat supply, and the second related to high wind speed during nighttime. Mor et al. (2018) examined the effect of water surface salinity on the evaporation by simultaneous measurements over a diluted, low-salinity, plume and over the highly saline brine of the open lake. Metzger et al. (2018) compared eddy covariance evaporation measurements with modeling during one year. Due to lack of actual measurements of the water surface and column temperatures, and radiation from the water surface, they utilized several assumptions. These enabled indirect calculations of water surface temperature, vapor pressure difference and energy budget components, which were later used for the evaporation models.

The above review shows that as yet, whole-year seasonal and diurnal patterns of evaporation and heat fluxes in the Dead Sea still call for a systematic study with direct measurements. We hypothesize that the synoptic- and mesoscale atmospheric circulations will affect evaporation in different manners. Hence the objectives of this study are:

(i) Characterize the seasonal and diurnal variations of evaporation and heat fluxes over the Dead Sea, and their forcing hydro-meteorological variables, during a whole year, by means of direct measurements over two consecutive years.
(ii) Investigate the applicability of various evaporation models for the deep hypersaline Dead Sea.

2. Methods

2.1. Sites and sensors

Measurements were conducted from onshore and offshore stations at the Dead Sea (Fig. 1), as described below. Measurements were made during 2 years, from March 2015 to April 2017, with some gap periods as depicted below.

2.1.1. Onshore station

The onshore station, hereafter denoted as Mishmar coastal station (MS), was located at the waterline (1–20 m onshore), on the tip of an elongated peninsula at the west coast of the lake (239863, 588405 ITM; Fig. 1b). The station was equipped with an eddy covariance system measuring evaporation rate (E) and sensible heat flux (H). The sensors were mounted 4.33 m above the water surface on an aluminum tower, anchored to the shore salt bed (Fig. 1c).

The eddy covariance system consisted of a three-dimensional sonic anemometer (WindMaster Pro; Gill Instruments Ltd., UK) and an open-path carbon dioxide/water vapor (CO_2/H_2O) infrared gas analyzer (IRGA; model LI 7500RS, LI-COR, Inc., USA). The 20 Hz raw data were processed and corrected to obtain half-hourly eddy fluxes using the EddyPro software by LI-COR. Most data processing was done on-site using the Smart-Flux system by LI-COR with embedded EddyPro software.

Eddy fluxes were measured from 29/MAR/2015 until 3/APR/2017. Gaps in data collection caused by instrument failure and repair are 17%, mainly during the intervals 26/OCT/2015-30/DEC/2015 and 04/APR/2016-31/MAY/2016. From the available data, 72% is considered valid flux measurements; the 28% of invalid measurements are due to: (i) 17.8% – wind directions from land (between azimuth of 180–300 degrees clockwise), and (ii) 10.2% – data flagged by EddyPro as low quality due to unsteady conditions. Only valid data were used in the following analyses.

Other meteorological variables measurements at the station were conducted with an air temperature (T_a) and relative humidity (RH) probe (model EE181; Campbell Scientific, Inc., USA) and a two-dimensional sonic anemometer (WindSonic; Gill Instruments, Inc., UK), which measured every 5 s and recorded the 10 min averages of mean wind speed and direction. Meteorological variables were recorded on a data logger (model CR1000; Campbell Scientific, Inc., USA). The latter instruments are identical to those on the offshore station (as described below) and enable comparing the data from both stations.

2.1.2. Offshore station

A meteorological buoy (EG100, Fig. 1b, 1d), located about 5 km northeast of the onshore station (241500, 593059 ITM), measured air temperature, air humidity and wind speed and direction, using similar sensor types and recording intervals as the onshore station. In addition, the buoy measured radiation fluxes at a height of 2 m above water surface, for calculating net radiation, (R_n) (CNR4; Kipp & Zonen B.V., The Netherlands); water surface temperature (T_s) using an infrared radiometer (SI-4H1; Apogee Instruments, Inc.) at 3 m above water surface; and water temperature profile of the upper 40 m using a thermistor chain (12–19 thermistors, data averaged every 20 min). We found that the offshore station well represented the onshore station, as was indicated by the close relation between U, T_a, and RH at the two stations (Lensky et al., 2018).

2.2. Data analysis

The vapor pressure difference, (Δe, Eq. (1)) is calculated using measured Dead Sea water activity, $\beta = 0.65$ (Mor et al., 2018), measured water surface and air temperatures and relative humidity. The Magnus-Tetens formula is used for the saturation vapor pressure:

$$e_{sat}(T) = 6.105 \cdot \exp\left(\frac{17.27 \cdot T}{T + 237.7}\right) \quad (2)$$

where T is temperature in °C and e_{sat} is in mbar (Barenburg, 1974).

The half hourly flux data obtained by the EddyPro software was further processed for different purposes: (i) a mean diurnal course was calculated as half hourly average of 7 days; (ii) the seasonal variation of the diurnal course was characterized similarly, but along their variations within the seasonal course; (iii) the seasonal variation of the daily average evaporation (and other fluxes) was calculated as the sum of the 48 half hours a day, and was further smoothed using a 7 day window moving average. Every error bar presented in this work represents the standard deviation normalized by $n - 1$, where n is the number of data entries being averaged.

For the estimation of the heat storage change (G), we divided the lake water body into horizontal layers assuming uniform temperature in each layer. The measured temperature using the 19 thermistors along the 40 m was interpolated to 40 layers, one meter thick. The total heat storage of the lake (Q_t) is the sum of the layers' heat storage, where the heat storage of the *i'th* layer (Q_i) was calculated by:

$$Q_i = \rho_{DS} \cdot Cp_{DS} \cdot T_i \cdot A_i \cdot z_i \quad (3)$$

where Dead Sea water density is, $\rho_{DS} = 1244\,\mathrm{kg\,m^{-3}}$ (Arnon et al., 2016; Sirota et al., 2016), heat capacity of the Dead Sea brine, $Cp_{DS} = 3030\,\mathrm{J\,kg^{-1}K^{-1}}$ (Steinhorn, 1981), T_i is the water temperature of the layer in K, A_i is the area of the layer normalized by the water surface area and z_i is the layer's thickness. The monthly heat storage change, $G = \frac{dQ_t}{dt}$, was calculated according to the best fit linear slope of the total heat storage. For the diurnal course of G, we used a moving mean of four hours and the maximal depth for integration was chosen as 15 m, in order to reduce the impact of internal waves on the calculations of G (Arnon et al., 2014); for more details see (Lensky et al., 2018).

3. Results

3.1. Measurements

3.1.1. General presentation of measured data

Figs. 2 and 3 below present, in two different manners, the whole two years measured and analyzed data set, including meteorological and limnological measurements, evaporation and heat fluxes. Later, Figs. 4 and 5 present diurnal courses of selected variables during typical seasons.

Seasonal and diurnal variations of the governing meteorological conditions, evaporation and energy fluxes are shown in Fig. 2, based on half hourly averaged data. In Fig. 2, horizontally correlated regions (horizontal 'continuous stripes') are evidence for a diurnal course that is repeatedly maintained by atmospheric meso-scale flows along the summer season, whereas vertically correlated regions (vertical 'stripes') indicate events lasting longer than a day, representing synoptic-scale events (see introduction).

Fig. 3 presents monthly means daytime and nighttime values of the sensible and latent heat fluxes, meteorological variables ($T_s - T_a$, U, Δe), and monthly means of net radiation and heat storage change. Fig. 3 is a more intuitive and conventional plot however Fig. 2 provides the entire dataset, so these figures are complementary. Fig. 3 provides another perspective to determine the dominance of the diurnal (separation of day and night) and seasonal cycles. In this study, nighttime is defined as the period where the incoming solar radiation (S_0) is negligible ($< 0.5\,\mathrm{W\,m^{-2}}$). Monthly averaged values of the measured meteorological variables are shown in Tables 1 and 2 (appendix).

3.1.2. Climatic and meteorological conditions – seasonal and diurnal variations

The net radiation is characterized by seasonal and diurnal cycles (Fig. 2a). The seasonal course has a typical sinuous shape (Fig. 3f), with monthly averages ranging from $\sim 20\,\mathrm{W\,m^{-2}}$ in December to $\sim 220\,\mathrm{W\,m^{-2}}$ in June. The diurnal cycle is characterized by positive values during daytime with maximum values at midday, and nighttime negative values. The seasonal and diurnal patterns of wind speed (U) are presented in Fig. 2e and Fig. 3b. During summer, the diurnal cycle dominates with high winds at night and low wind speed during the day. This diurnal pattern is attributed to the Mediterranean Sea Breeze – a mesoscale circulation system induced by the daytime differential surface heating between land and (Mediterranean) Sea. The sea breeze front reaches the Dead Sea at sunset and blows during night as dry and warm northerly wind (Alpert et al., 1997; Gertman and Hecht, 2002; Lensky and Dayan, 2012; Lensky et al., 2018). During winter, synoptic scale circulation patterns alternate typically every few days, with periods of strong winds ($> 6\,\mathrm{m\,s^{-1}}$) that last over a day (vertical stripes in Fig. 2e). Therefore, the wind diurnal cycle during winter is not dominant (Fig. 3b). The seasonal variation of the monthly mean wind speed is apparent only through the diurnal cycle: prominent in the summer, disappearing in the winter (Fig. 3b).

Air temperature is characterized by a seasonal cycle with an amplitude larger ($\Delta T > 16$°C) than the diurnal cycle ($\Delta T < 5$°C) (Fig. 2b). Winter daily maximum is in the afternoon and summer daily maximum is at sunset. The monthly averaged T_a (Table 1), varied with a typical seasonal sinuous pattern. These observations are consistent with the long term four decadal measurements from the buoy EG100 (Gertman and Hecht, 2002; and the database of I. Gertman). It is notable that the second winter was colder than the first (note color index in Fig. 2b). Both seasonal and diurnal courses of air temperature show a lagged response to R_n due to the thermal inertia of the air; while the diurnal cycle is also subject to the effect of the retarded arrival of Mediterranean Sea breeze (see hereafter).

Water surface temperature (Fig. 2c) exhibited diurnal and seasonal cycles, similar to air temperature behavior. The diurnal and seasonal variations of T_s are moderated compared to T_a; additionally, T_s lags T_a in the seasonal scale (< month). These effects are attributed to the high thermal inertia of the lake water.

3.1.3. Water heat storage change

The water heat storage change (G, Eq. (3), Fig. 2i) is characterized by seasonal and diurnal cycles, with high heat flux values ($\pm 1000\,\mathrm{W\,m^{-2}}$), similar to R_n. The seasonal cycle of G is in phase with R_n (Fig. 3f), however, it remains positive for two months after R_n has reached its maximum in June, indicating that the lake is still heating even though R_n is already diminishing (also observed in T_s). The diurnal course of G along the warm season is characterized by positive values during the daytime and negative values at nighttime, indicating that the lake is storing energy during the day and dissipating it during the night. The amplitude of the diurnal cycle varies seasonally, similarly to R_n (i.e. the red strip narrows toward the winter in Fig. 2i). In winter, the lake is vertically homogeneous and the dominance of the diurnal pattern of G is reduced (blue domains in Fig. 2i).

3.1.4. Vapor pressure difference

The vapor pressure difference (Δe) seasonal and diurnal patterns are presented in Fig. 2d and Fig. 3a. A diurnal cycle is dominant in summer with a triple peak, in the morning, afternoon and evening, with higher values during daytime. In winter and in the transition seasons, the diurnal cycle is not evident, since different synoptic conditions dominate. The seasonal cycle presents a summer peak and a winter peak. Overall the vapor pressure difference in this hyper-arid environment remained positive along the entire observation period.

3.1.5. Vapor transport agents

The major vapor transport agents are the wind, represented here by wind speed (Section 3.1) and the thermal stability of the air overlying the water surface. The temperature difference between the water

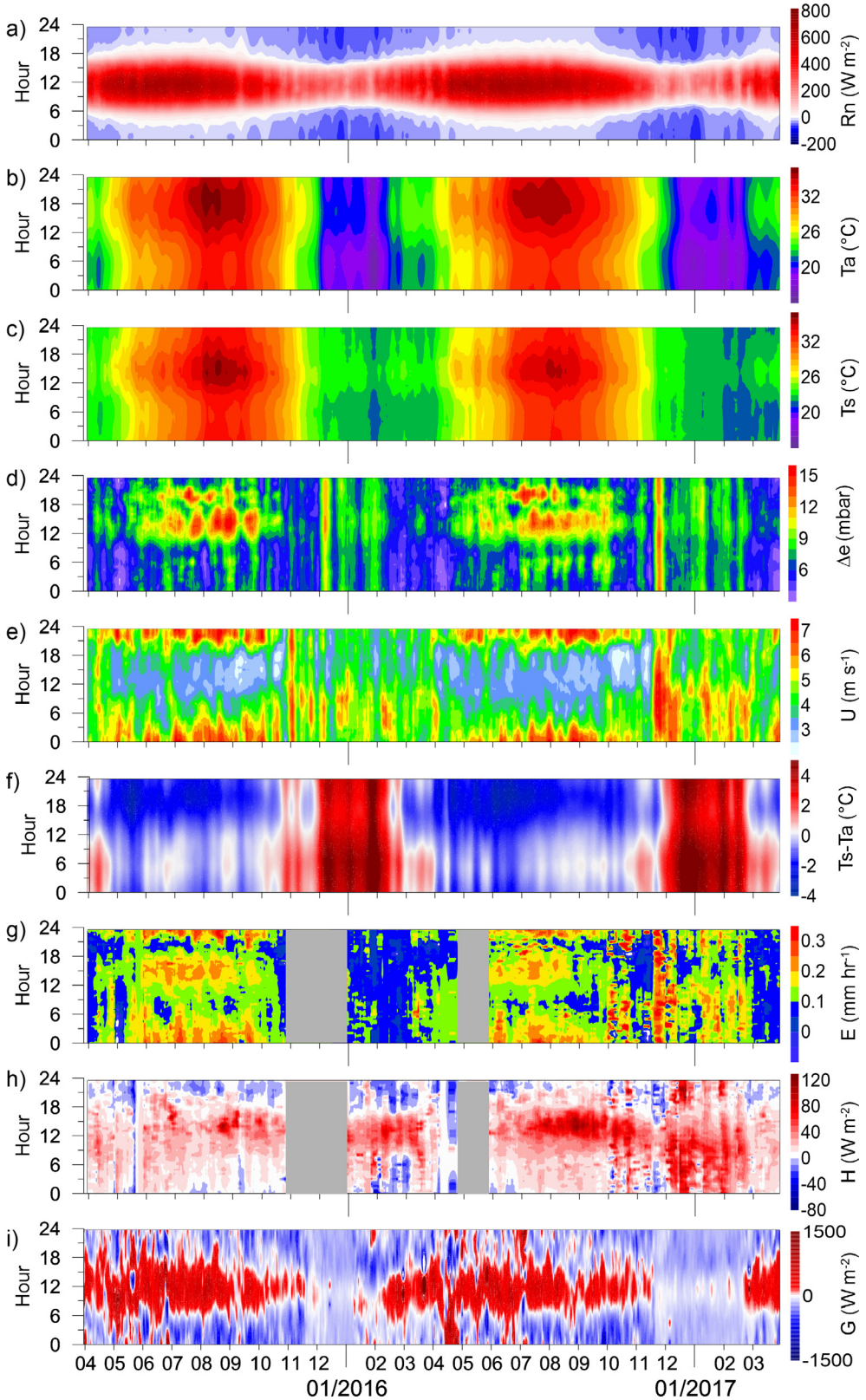

Fig. 2. Diurnal and seasonal variations (y and x axes, accordingly) during two years of measurements. (a) Net radiation (R_n), (b) air temperature (T_a), (c) water surface temperature (T_s), (d) vapor pressure difference (Δe) (e) wind Speed (U) (f) temperature difference between water surface and overlying air ($T_s - T_a$) (g) evaporation rate (E), (h) sensible heat flux (H) and (i) heat storage change (G). All parameters are based on half hourly means. Color scale is in the right of each panel.

surface and the air is an indicator of the thermal stability of the air above the water surface (Assouline and Mahrer, 1993). Positive values (red color in Fig. 2f) are related to unstable conditions that enhance mixing and turbulence of the air above the water, while negative values (blue color) represent stable conditions, which diminish these effects. These processes are significant in transporting vapor from the water

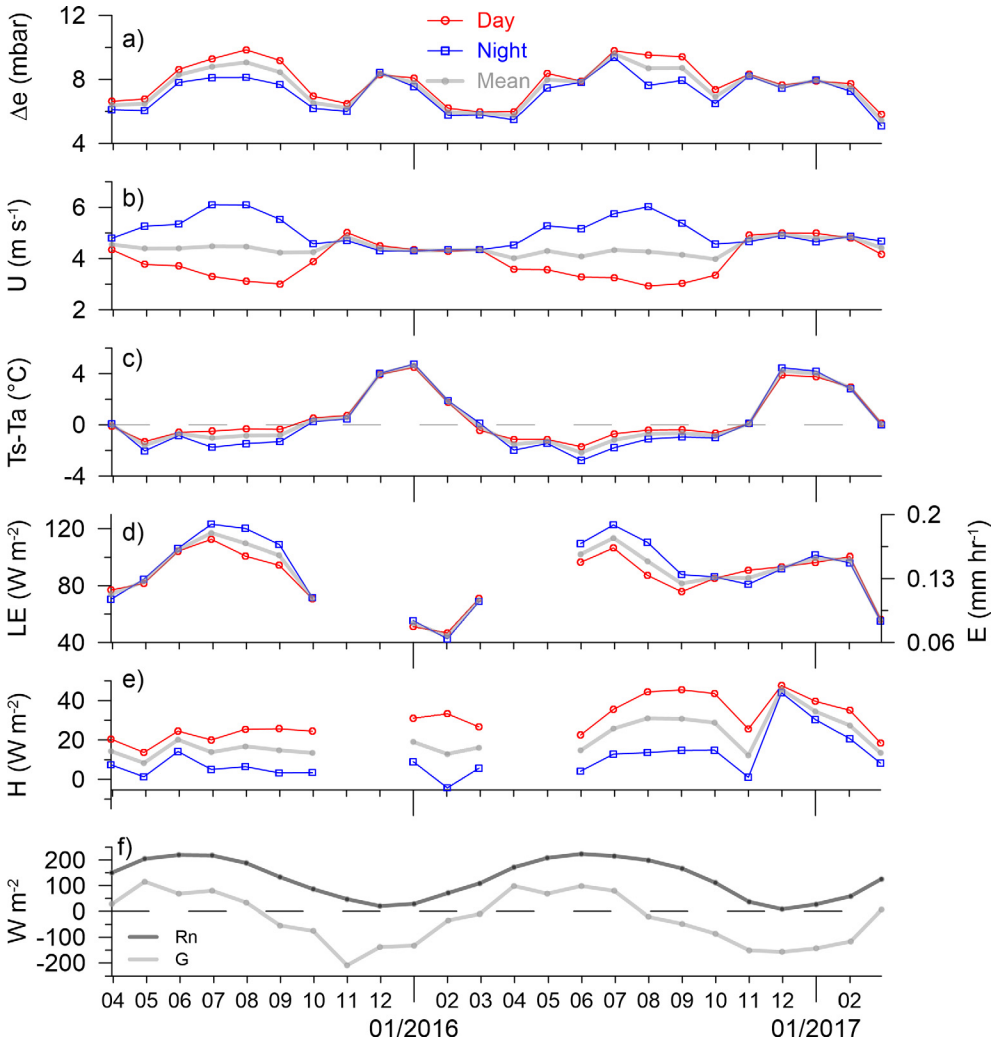

Fig. 3. Average monthly daytime and nighttime values of (a) vapor pressure difference, (b) wind speed, (c) temperature difference between the brine and the overlying air, (d) latent heat flux, (e) sensible heat flux, and (f) monthly means of net radiation and heat storage change. Gray line is the monthly average without day/night classification. Gaps are due to months with less than 50% of valid data.

surface and enhancing or depressing evaporation (Assouline and Mahrer, 1993). During winter, $T_s - T_a$ is positive (red regions in Fig. 2f) along the diurnal cycle. Hence, during winter, a destabilizing vertical temperature gradient is generated between the water surface and the cool air which may enhance evaporation rate. It is notable, that $T_s - T_a$ was greater during the second and cooler winter of measurements (Dec 2016, Jan-Feb 2017) due to lower air temperature. In the warm season, $T_s - T_a$ is mostly negative (blue domains) with more negative values during nighttime than daytime (Fig. 3c). During summer evenings warm air increases thermal stability, which may explain the low evening evaporation in spite of the peak in Δe (see discussion).

3.1.6. Evaporation

To analyze seasonal and diurnal cycles of evaporation, in addition to Fig. 2g and Fig. 3d, we plotted in Figs. 4 and 5, data from three seasonal regimes: Summer (Jun-Sep), winter (Dec-Feb), and transition seasons (Mar-May, Oct-Nov).

In summer, a diurnal cycle dominates, with a clear double-peak: an evaporation peak at night and a second peak in the afternoon (horizontal stripes in Fig. 2g, Fig. 4a). This phenomenon that was analyzed in detail by Lensky et al. (2018) based on one week of observations, and is validated here based on data from the entire summer season.

During winter, when the synoptic scale atmospheric circulation patterns are much more dominant than the mesoscale flow, there is no evident repeated diurnal cycle (vertical stripes in Fig. 2g, Fig. 4c). Consequently, due to the different synoptic events, the winter diurnal patterns are different in the two consecutive years, unlike the summer diurnal patterns that are reproduced each year.

In the transitional seasons, a gradual change in the diurnal patterns from winter to summer prevails with a small evaporation peak in the morning and a daily maximum at night (Fig. 4d). During autumn (Oct–Nov), as the daytime differential surface heating between land and sea weakens, the Mediterranean Sea breeze weakens (Lensky and Dayan, 2012), as well as the night evaporation peak (Fig. 4c). Due to the nature of synoptic influence in winter and transition seasons, it is notable that the diurnal cycles of E, $T_s - T_a$, Δe, U have a weaker variation, as is indicated in Fig. 4b,c,d – the diurnal amplitude is within their standard deviation error. Fig. 5 presents averaged monthly diurnal courses of the net radiation and heat storage change, and the latent and sensible heat fluxes.

In the seasonal time scale, evaporation is high in summer, with a clear peak in the summer months, which is evident in both years, with average maximum E in July of 0.174 mm hr^{-1}. During winter evaporation is variable: since it is subject to synoptic events it can have either high values (i.e. January 2017: 0.144 mm hr^{-1}) leading to evaporation winter peak (in addition to summer peak), or have low values (i.e. January 2016: 0.065 mm hr^{-1}). During the transition seasons, evaporation was low. These monthly-means accumulate to a two-year

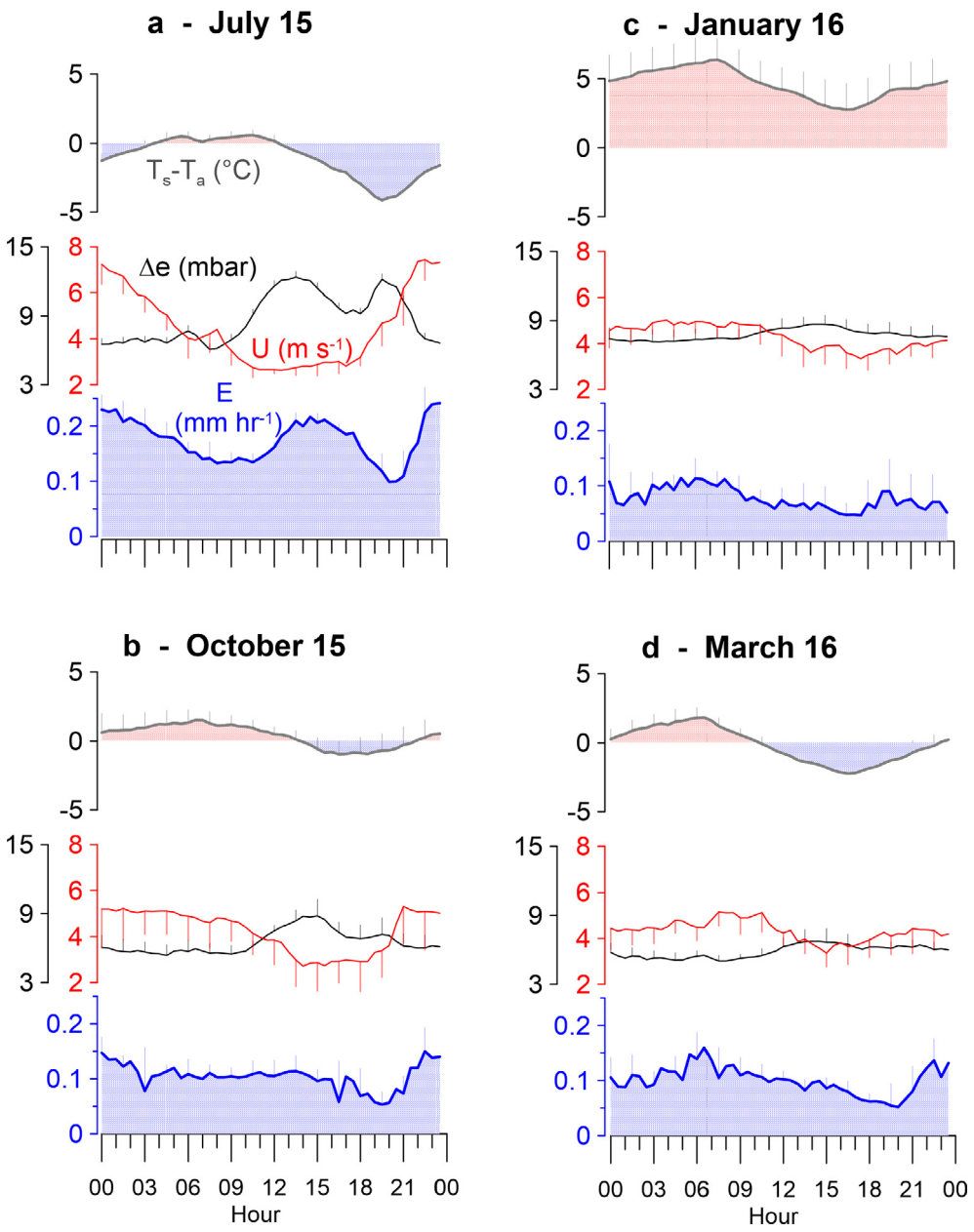

Fig. 4. Averaged monthly diurnal courses of evaporation (blue), vapor pressure difference (black), wind speed (red) and temperture difference between water surface and overlying air (gray) of four representitive months (July and October 2015, January and March 2016). (For interpretation of the references to color in this figure legend, the reader is referred to the web version of this article.)

mean annual evaporation rate of 1.13 m yr^{-1} (± 0.13 mm hr^{-1}).

3.1.7. Sensible heat flux

The sensible heat flux (H) is the lowest among the major fluxes (Fig. 3e and Fig. 5). H is characterized by a diurnal cycle with daytime positive values, peaking at afternoon, and nighttime negative values (Fig. 2h); excluding the winter of 2016/17 which was dominated by positive values throughout the diurnal cycle (Fig. 2h). The magnitude of the daily peak in H changes seasonally (Fig. 5): it is relatively low in summer (i.e. 30 W m^{-2} in July 2015, Fig. 5a) but larger in winter. During winter H peak reached the magnitude of LE peak (i.e., about 50 W m^{-2} in January 2016, Fig. 5c). In December 2016, H increased and was positive through most of the day with highest monthly mean (Fig. 2h, Fig. 3e). With these changes between the two years, no typical seasonal cycle could be identified. Note that the sensible heat is not well correlated to T_s-T_a, as would be expected from flux-gradient law. We do not have a proper explanation for that, yet, we can hypothesize that this observation is related to the phenomenon of counter-gradient flux (Deardorff, 1966), i.e. a flux which is in opposite direction to the mean gradient of its driving force. This phenomenon may occur when transport is dominated by moving air parcels, not by the local scalar gradient, but this calls for a more systematic study on sensible heat, which is beyond the scope of this paper.

3.2. Evaporation models for hypersaline water surface

The estimates by different evaporation models are compared to evaporation rates measured by means of the eddy covariance system, E_{EC}, in order to evaluate their applicability to deep hypersaline waterbodies. The models are:

1) A *mass transfer model* (MT model) (Harbeck (1958)):

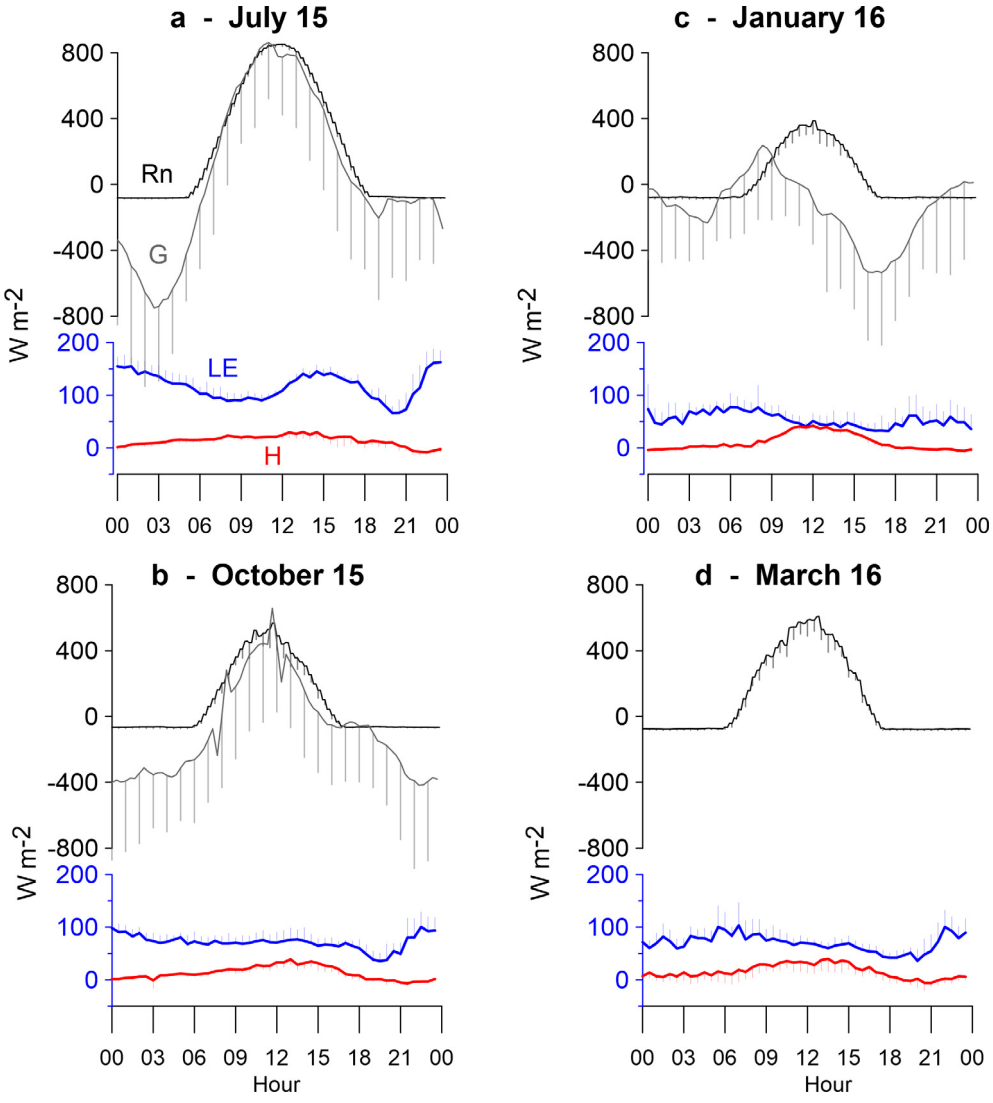

Fig. 5. Averaged monthly diurnal courses of lake surface energy fluxes: net radiation, latent heat of evaporation and sensible heat, and heat storage change, of four representitive months (July and October 2015, January and March 2016).

$$E_{MT} = N \cdot U \cdot \Delta e \quad (4)$$

where E_{MT} is the evaporation rate (mm hr^{-1}), N is the mass transfer coefficient, $U\,(ms^{-1})$ is the wind speed and $\Delta e\,(mbar)$ is the vapor pressure difference (Eq. (1)). This model inherently accounts for water salinity through Δe (Eq. (1)), and requires the calibration of the coefficient N.

2) A *modified Penman model* for hypersaline water surfaces (with a lowered water activity) developed by Calder and Neal, (1984) (CN model). This model takes into account the available energy (Rn-G) while the vapor pressure deficit (VPD) is corrected for the reduced activity of the saline water, β:

$$E_{CN} = \frac{\Delta(R_n - G) + \gamma(3.6 + 2.5U)(e_{sat}(T_a) - \frac{RH}{\beta} e_{sat}(T_a))}{L(\Delta + \gamma/\beta)} \quad (5)$$

Here, E_{CN} is the evaporation rate in mm hr^{-1}, δ (mbar °C^{-1}) is the rate of increase of saturation pressure with temperature, R_n and G (W m^{-2}) are the net radiation and water heat storage change, respectively, γ is the psychrometric constant ($mbar$ °C^{-1}), T_a is air temperature (°C), and e_{sat} (mbar) is saturation vapor pressure (Eq. (2)).

3) An *aerodynamic model* (AD) includes a transport coefficient, Ce, based on the logarithmic wind profile and the friction velocity derived from high frequency data (Brutsaert, 2005; Tanny et al., 2008):

$$E_{AD} = \frac{0.622}{\rho_w \cdot p} C_e \cdot \rho_a \cdot U \cdot 3.6 \cdot 10^6 \cdot \Delta e \quad (6)$$

$$C_e = \frac{k^2}{ln\left(\frac{z_2}{z_{0v}}\right) ln\left(\frac{z_1}{z_{0m}}\right)}$$

Here ρ_w and ρ_a denote water and air density (kg m^{-3}), U is wind speed (m s^{-1}), p is air pressure ($mbar$), z_1 and z_2 are the heights (m) of wind speed and vapor density measurements, respectively, and $z_{0m} = u_*^2/(81g)\,(m)$ is the momentum roughness length where $u_*(\mathrm{ms}^{-1})$ is the measured friction velocity, g is the gravitation acceleration (m s^{-2}), $k = 0.41$ is the Von-Karman constant and $z_{0v} = 7.4 z_{0m} \exp[-2.25(u_*/\nu)^{1/4}]$ (Brutsaert, 1982, Eq. (5.28) and p. 124), where ν (m^2 s^{-1}) is air kinematic viscosity. Here too, the impact of water salinity is expressed through Δe (Eq. (1)).

Fig. 6 present the monthly average evaporation rates, measured and calculated, along the two years observation period. The MT model was calibrated by calculating the mass transfer coefficient, N, that best fits

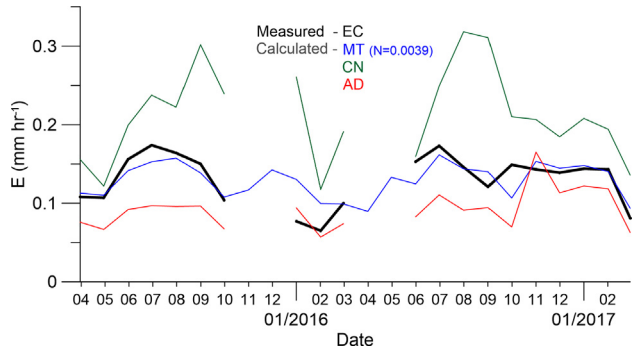

Fig. 6. Measured (EC) and calculated (MT, CN and AD) monthly means of evaporation (black and colored, respectively). Gaps are due to months with less than 50% of valid data. See text for MT models with dashed and solid parts of the curves. Note the higher correlation of MT model to the measured data.

the monthly averaged measured evaporation (E_{EC}) with the monthly averages of measured $U{\cdot}\Delta e$. The best fit for the entire data set is $N = 0.0039 \pm 0.0001$ with $R^2 = 0.97$ (we also split the dataset to a first year of calibration and second for validation, and vice versa, which yielded very similar results: $N = 0.0040$, $R^2 = 0.97$ and $N = 0.0038$, $R^2 = 0.98$, respectively).

Fig. 7 presents regression of daily averages for the whole period of calculated evaporation based on the three models (E_{MT}, E_{CN}, E_{AD}) versus the measured evaporation, E_{EC}, including quantifiable correlation indexes. The calibrated mass transfer model, $E_{MT\ (N=0.0039)}$, matches best the observations (slope = 1.05); however it overestimates in cases of low measured evaporation rates (partly in unstable thermal stability conditions). The aerodynamic model, E_{AD}, underestimates measured data by about thirty percent (slope = 0.69); E_{AD} closely fits E_{EC} at low values. The AD model uses friction velocity derived from high frequency wind speed measurements. The need of measuring the friction velocity is a disadvantage for a practical evaporation formula, since common meteorological stations does not include sonic anemometers that are required for such measurements. The modified Penman model, E_{CN}, overestimated the daily evaporation by 150%. Besides, it is less suitable due to the inclusion of G, the stored heat flux in the lake, whose measurement is prone to large errors and is not available from routine measurements. To summarize, the mass transfer (MT) model with $N = 0.0039$, best matches the observations; besides, it is a simple formulation, based on common meteorological data and therefore an excellent candidate for management of water resources.

4. Discussion

4.1. Available energy for evaporation

The Dead Sea is a deep lake and thus has a large heat capacity. The heat stored in the lake water is used for evaporation and sensible heat flux. Net radiation is the primary energy source for heating the water body; R_n daily averages are positive along the year, whereas the heat storage change alternates seasonally from positive to negative values. The water body gained heat from March until July and lost heat from August to February, approximately (Fig. 3f). In addition, our results showed that evaporation rates in the two consecutive winters could vary in magnitude ($0.065\ mm\ hr^{-1}$ in January 2016 and $0.144\ mm\ hr^{-1}$ in January 2017). These observations suggest that the Dead Sea operates as a source of stored energy, available for evaporation and sensible heat flux even in times of low net radiation, hence all year long, including nighttime and winter. Winter evaporation rate may vary annually depending on surface weather events associated with the varying synoptic scale atmospheric circulation patterns; while in summer, the evaporation rate is annually uniform, as the Persian trough is steady along the summer, giving place to the mesoscale flows as the Mediterranean Sea Breeze.

4.2. Evaporation peaks – environmental controls and timing

The vapor pressure difference in the Dead Sea is constantly positive, and hence without any transport resistance, evaporation is expected to follow Δe pattern at any time scale. However transport resistance plays a major role on evaporation. Diurnal evaporation patterns vary seasonally:

In summer (Jun-Sep), the synoptic circulation is stable providing weak background wind velocity (Persian trough), thus the diurnal Mediterranean Sea Breeze (mesoscale circulation) is the dominant wind pattern. Evaporation is temporally correlated by the vapor pressure difference and the transport mechanism of the vapor (i.e. wind speed), resulting in a double peaked pattern. The first E maximum results from the high noontime net radiation and is associated with the daily peak of Δe in the afternoon while the second E maximum is attributed to the nightly high wind speed as shown in Fig. 4a, and for two summers in Fig. 2. The evening evaporation is suppressed by thermally stable conditions in spite of Δe peak.

In winter (Dec-Feb), as sunlight duration shortens and its intensity weakens, the diurnal cycles weaken and are undetected with respect to the dominant synoptic scale circulation. Continuous positive Δe and thermal instability (Fig. 2f; Fig. 3c; Fig. 4c) along with events of high

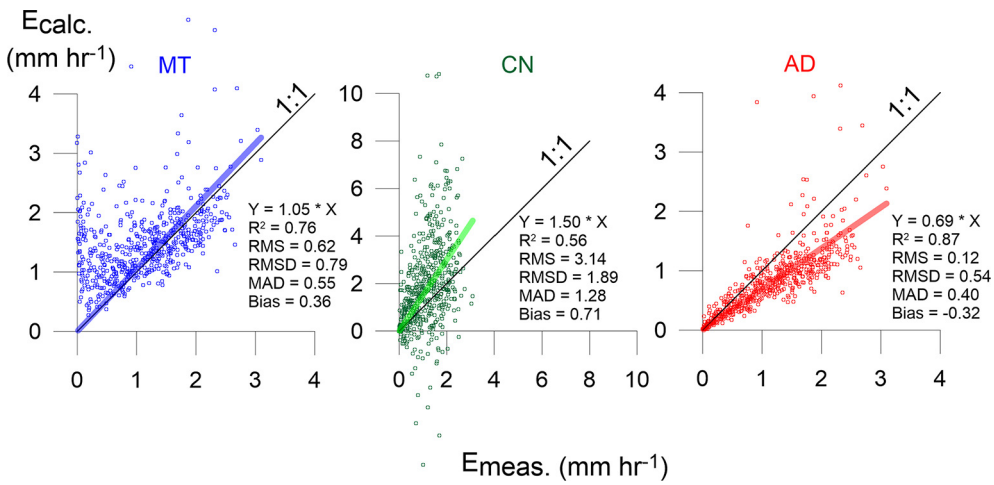

Fig. 7. Calculated evaporation rates based on three models versus EC measured, daily averages. RMS – root mean square, RSMD - root mean square difference, MAD – mean absolute difference.

wind speed associated with synoptic scale atmospheric circulation, induce evaporation regardless of the time of day, resulting in small difference between nighttime and daytime (Fig. 3d). These synoptic events may last several days with high wind speed and high evaporation rate (vertical 'columns' in Fig. 2e; Fig. 2g), and change the winter average monthly mean of evaporation (Table 1). Since summer evaporation was nearly the same in the two years of measurements, winter changes in evaporation are accountable for the change in total evaporation between the years.

Transitional seasons are also subject to synoptic scale events: In spring (Mar-May), while the nighttime boundary layer is thermally unstable (Fig. 2d) there is an increase in the night peak and gradual transition from winter patterns to summer-like diurnal course. In autumn (Oct-Nov) there was only a morning peak temporally correlated with a daily maximum in wind speed. Hence, during the transition seasons the evaporation is dependent on wind speed as the daily cycles of E follow those of U and the evaporation peaks are aligned with wind speed peaks (Fig. 4b; Fig. 4d).

4.3. Wind controls the diurnal evaporation course, limited by thermal stability

In the diurnal time scale, there is a good temporal correlation between the evaporation rate and wind speed (Fig. 2; Fig. 4). In summer, as the strong winds are at night, nighttime evaporation is higher than daytime (e.g. 0.181 mm h^{-1} vs 0.150 mm h^{-1} in August 2015), and is, thus, a large contributor to annual water loss from the Dead Sea. In the summer evenings, the vapor pressure difference and wind speed are high, yet, evaporation is at its lowest. At this time of day, the Mediterranean sea-breeze brings warm air, so the thermally stable boundary layer (Fig. 4a; Fig. 2d), inhibits evaporation (similar effect was documented by Assouline and Mahrer (1993)). Later, the sea breeze cools down, thermal stability decreases and evaporation rate increases. The superposition of wind speed and vapor pressure difference might result in high evaporation rates, but the thermal stability plays a significant role. Thermal stability can reduce evaporation, like in summer evenings, or enhance evaporation like in the winter, when the boundary layer is constantly thermally unstable. Based on these observations, it seems that wind regime and boundary layer properties dominate the diurnal evaporation cycle in the Dead Sea.

4.4. Measured and modeled evaporation: relations with forcing variables

Diurnal courses of measured and modeled evaporation rates, are presented in Fig. 8 in order to relate them to the governing processes. We present the monthly averaged diurnal course of July 2015, characterized by double diurnal evaporation peak, as presented by Lensky et al. (2018) for one week, and in the present paper it is expanded to the entire season. To illustrate the relation between the governing meteorological factors and the resulted evaporation, we present in Fig. 8 also the temperature difference between water and overlying air, vapor pressure difference, wind speed, net radiation and stored water heat flux. At the diurnal time scale, all three models could not reliably reproduce the diurnal course of measured evaporation. Here again, $E_{MT\ (N=0.0039)}$, seems to provide the best simulation of the measured evaporation, E_{EC}. However, in the evening, E_{MT} predicts an evaporation peak instead of the actual night peak, since it does not take into account the thermal stability (see the negative vertical temperature difference in the top panel) which inhibits evening evaporation. The modified Penman model, E_{CN}, over estimates evaporation with a very large peak at ~3AM, which is related to the large *Rn-G* (Fig. 8). This overestimate

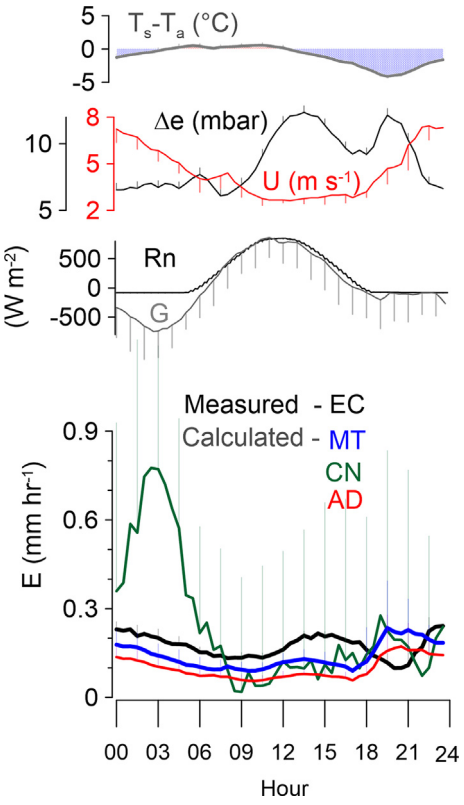

Fig. 8. Diurnal course of measured and calculated evaporation, monthly averaged for July 2015. Calculated evaporation is based on mass transfer model (MT), Penman model for the Dead Sea – Calder and Neal (1984) (CN), and aerodynamic model (AD). Also presented are, from top to bottom, measured temperature difference between water surface and air, vapor pressure difference, wind speed and the radiative and stored heat fluxes.

appears to be caused mainly by the very large (and negative) G (Fig. 8); note that G has very large error bars, illustrating the difficulty in a reliable estimation of this term in a deep hypersaline lake like the Dead Sea. Hence, it suggests that Penman type models, which include the energy storage term, are less reliable for evaporation estimates in such large, deep, and hypersaline water bodies. The aerodynamic model, E_{AD}, generally underestimates evaporation and follows the daily course pattern, except for overestimating evaporation in evening instead of during nighttime, similar to the E_{MT}. Although E_{AD} is based on measured friction velocity (through the roughness length term in *Ce*) which represents the turbulence of the flow, it does not take into account explicitly the atmospheric stability, induced by the negative temperature difference, since *Ce* assumes neutral stability. Therefore, it overestimates evaporation during evening.

4.5. Vapor pressure difference controls the seasonal evaporation cycle

On the seasonal time scale, patterns of vapor pressure difference are temporally correlated to those of measured evaporation and evaporation models estimations (Fig. 3a,d, Fig. 6 respectively). This correlation is also valid for the calculated evaporation using the mass transfer model. The vapor pressure difference dominates the seasonal variations in evaporation, with possible inter annual differences between winters that are attributed to the magnitude of synoptic events.

5. Conclusions

Evaporation from the Dead-Sea was measured directly with an eddy covariance system during a two-year period, along with corresponding energy fluxes and meteorological variables. Data is analyzed on diurnal and seasonal timescales. The following main conclusions can be drawn from this study:

1. The Dead Sea stores heat during the day, providing energy for evaporation at night in summer, and stores heat during summer, providing heat for evaporation in winter.
2. The annual rate of evaporation from the Dead Sea is 1.13 m yr^{-1}, with a significant contribution of nighttime evaporation in summer and during winter.
3. Evaporation in the Dead Sea is governed by vapor pressure difference in the seasonal time scale and wind speed in the diurnal time scale.
4. Thermal stability of the overlying boundary layer is also a significant factor on evaporation: stable conditions can depress the evaporation rate, despite high wind and vapor pressure difference.
5. After being calibrated and validated against measured data, the mass transfer model gives a good estimation for monthly evaporation rate and can be applied for the Dead Sea brine using: $E_{MT} = N{\cdot}U{\cdot}\Delta e$, $N = 0.0039 \pm 0.0001$.

Acknowledgments

We thank the two anonymous reviewers, Associate Editor Di Long and the Editor-in-Chief Marco Borga for insightful comments that significantly improved the manuscript. We thank the Geological Survey of Israel team for the intensive field and lab assistance: Raanan Bodzin, Hallel Lutzky, Uri Malik, Alon Peretz, Ali Arnon, Ido Sirota, Haggai Eyal and Yohai Magen. Tal Ozer and Boris Katsenelson from Israel Limnology and Oceanographic Research for field assistance and maintenance of the meteorological buoy. Denis Kuchuk from Meteo-Tech for technical support with the eddy covariance system; Taglit R/V team—Silvy Gonen, Shahar Gan-El and Meir Yifrach for operating the R/V in the harsh conditions of the Dead Sea for install and maintenance of the stations. The research was funded by the Israeli Government under GSI DS project 40572. N.G.L. is involved in the PALEX project "Paleohydrology and Extreme Floods from the Dead Sea ICDP core", funded by the DFG (grant no. BR2208/13-1/-2).

Appendix A. Table of monthly averaged meteorological variables and components of the surface energy budget

Table 1
Monthly averaged meteorological variables and components of the surface energy budget during the observation period: S_0: incoming solar radiation (W m^{-2}); R_n: net radiation (W m^{-2}); H: sensible heat flux (W m^{-2}); LE: latent heat flux (W m^{-2}; G: the heat storage change in the water body (W m^{-2}); U: wind speed (m s^{-1}); RH: relative humidity (%); T_a: air temperature (°C); T_s: water surface temperature (°C); ΔT: temperature difference between the water surface and the air ($T_s - T_a$, °C); e_a: vapor pressure in the atmosphere (*mbar*); e_s: vapor pressure at the water surface (*mbar*); Δe: vapor pressure difference between the water surface and the atmosphere (*mbar*); E: evaporation rate (mm hr^{-1}). S_0, R_n and T_s were measured at EG100 station, all other parameters at *MS* station.

Months	S_0	R_n	H	LE	G	U	RH	T_a	T_s	ΔT	e_a	e_s	Δe	E
April	243.9	150.6	14.3	73.9	28.2	4.54	43.9	24.1	24.0	0.0	13.04	19.41	6.37	0.108
May	300.1	205.2	8.3	82.9	116.0	4.39	43.9	28.9	27.2	−1.6	17.10	23.54	6.44	0.107
June	312.6	220.1	20.1	104.9	68.3	4.40	44.4	30.7	30.0	−0.7	19.26	27.50	8.25	0.156
July	311.9	217.8	13.8	116.9	80.4	4.47	44.5	33.1	32.1	−1.0	22.24	31.00	8.76	0.174
August	271.9	188.6	16.8	109.6	34.3	4.47	46.3	35.0	34.1	−0.8	25.74	34.76	9.03	0.164
September	212.3	133.7	14.8	101.2	−53.8	4.22	46.4	34.0	33.1	−0.8	24.48	32.89	8.42	0.150
October	162.5	86.6	13.4	71.2	−75.6	4.25	51.5	30.0	30.4	0.4	21.70	28.21	6.51	0.104
November	128.1	47.4			−209.3	4.84	48.6	25.3	25.9	0.6	15.57	21.77	6.19	
December	119.7	20.4			−138.0	4.38	45.4	19.2	23.2	4.0	10.14	18.47	8.34	
January	118.9	29.4	19.0	53.5	−132.6	4.31	48.9	18.0	22.6	4.6	10.04	17.80	7.75	0.077
February	165.5	71.3	12.9	44.6	−33.9	4.31	48.8	21.0	22.8	1.8	12.05	17.98	5.93	0.065
March	202.4	109.7	16.2	69.9	−9.4	4.34	44.0	23.1	23.0	−0.2	12.33	18.18	5.85	0.100
April	266.2	172.0			98.9	4.01	43.8	26.7	25.2	−1.5	15.06	20.80	5.73	
May	297.6	208.4			69.1	4.29	40.6	28.8	27.5	−1.3	15.86	23.81	7.95	
June	315.3	224.0	14.6	102.0	98.8	4.08	41.9	32.6	30.5	−2.2	20.52	28.35	7.83	0.153
July	303.6	215.9	25.8	113.3	80.0	4.33	43.6	34.3	33.1	−1.2	23.32	32.89	9.57	0.173
August	279.6	199.4	31.0	97.3	−20.6	4.26	46.7	34.3	33.6	−0.7	25.05	33.72	8.66	0.146
September	251.3	167.0	30.8	81.5	−48.2	4.14	45.0	32.4	31.8	−0.7	21.75	30.42	8.68	0.121
October	205.3	111.6	28.8	85.7	−85.8	3.97	45.8	29.7	28.8	−0.8	18.86	25.75	6.89	0.149
November	139.7	37.0	12.2	85.5	−150.8	4.77	38.9	25.0	25.1	0.1	12.46	20.70	8.24	0.143
December	105.9	8.7	45.7	92.5	−157.0	4.94	50.0	18.9	23.1	4.2	10.81	18.32	7.51	0.139
January	121.3	27.5	34.5	99.1	−143.5	4.80	46.0	18.4	22.4	4.0	9.67	17.57	7.91	0.144
February	162.5	59.1	27.4	98.0	−116.7	4.83	44.0	19.0	21.8	2.9	9.53	16.98	7.45	0.143
March	200.5	125.9	13.4	55.8	6.6	4.42	45.5	22.4	22.4	0.0	12.19	17.62	5.43	0.081
Mean	216.6	126.5	20.7	87.0	−28.9	4.4	45.4	26.9	27.2	0.4	16.61	24.10	7.49	0.130

Appendix B. Table of monthly averaged daytime and nighttime values of meteorological variables and components of the surface energy budget

Table 2
Monthly averaged daytime and nighttime values of meteorological variables and components of the surface energy budget in the observation period: *H:* sensible heat flux (W m^{-2}); *LE:* latent heat flux (W m^{-2}); ΔT*:* temperature difference between the water surface and the air (°C); Δe*:* vapor pressure difference between the water surface and the atmosphere (*mbar*); *RH*: relative humidity (%); *U*: wind speed (m s^{-1}). *Rn* and T_s were measured at EG100 station, all other parameters at *MS* station.

Months	*H*		*LE*		ΔT		Δe		*RH*		*U*		*E*	
	Day	Night	Day	Night	Day	Night	Day	Night	Day	Night	Day	Night	Day	Night
April	20.4	7.3	76.9	70.4	−0.1	0.1	6.61	6.09	43.3	44.6	4.34	4.78	0.112	0.103
May	13.7	1.3	81.6	84.6	−1.3	−2.0	6.75	6.02	44.1	43.5	3.77	5.26	0.111	0.102
June	24.5	14.2	104.1	106.1	−0.6	−0.8	8.59	7.78	44.3	44.4	3.70	5.33	0.155	0.158
July	20.1	5.0	112.5	123.1	−0.5	−1.8	9.25	8.08	45.2	43.6	3.30	6.10	0.167	0.183
August	25.4	6.5	100.7	120.1	−0.3	−1.5	9.81	8.09	46.6	46.0	3.11	6.08	0.150	0.181
September	25.7	3.2	94.2	108.7	−0.4	−1.3	9.15	7.64	46.7	46.2	3.00	5.53	0.140	0.161
October	24.5	3.4	70.7	71.6	0.5	0.2	6.92	6.17	51.3	51.7	3.87	4.57	0.103	0.104
November					0.7	0.5	6.46	5.98	48.4	48.8	5.01	4.70		
December					3.9	4.0	8.26	8.40	45.9	45.0	4.50	4.29		
January	31.0	9.0	51.1	55.4	4.5	4.7	8.06	7.51	47.5	49.9	4.34	4.29	0.074	0.080
February	33.3	−4.3	46.7	42.6	1.7	1.9	6.17	5.73	48.1	49.3	4.27	4.35	0.069	0.061
March	26.6	5.7	71.0	68.8	−0.4	0.1	5.94	5.76	43.2	44.8	4.35	4.34	0.104	0.097
April					−1.1	−2.0	5.97	5.46	44.3	43.2	3.58	4.52		
May					−1.1	−1.5	8.34	7.43	40.3	41.0	3.56	5.28		
June	22.5	4.2	96.4	109.5	−1.7	−2.8	7.86	7.80	43.2	40.2	3.27	5.15	0.144	0.164
July	35.6	12.8	106.3	122.5	−0.7	−1.8	9.75	9.33	44.6	42.3	3.25	5.75	0.159	0.191
August	44.4	13.6	87.3	110.3	−0.4	−1.1	9.48	7.60	46.3	47.3	2.92	6.02	0.133	0.163
September	45.4	14.7	75.7	87.8	−0.4	−1.0	9.39	7.90	44.6	45.4	3.02	5.37	0.113	0.130
October	43.6	14.8	85.1	86.2	−0.6	−1.0	7.34	6.46	45.5	46.0	3.34	4.56	0.142	0.155
November	25.6	1.0	90.9	80.9	0.1	0.1	8.29	8.19	38.9	39.0	4.90	4.65	0.149	0.139
December	47.7	44.0	93.3	91.8	3.9	4.5	7.63	7.42	48.6	51.1	4.99	4.89	0.147	0.132
January	39.7	30.4	96.3	101.4	3.8	4.2	7.85	7.95	45.8	46.2	4.98	4.65	0.141	0.147
February	35.1	20.7	100.4	96.0	2.9	2.8	7.72	7.22	43.3	44.6	4.80	4.86	0.145	0.141
March	18.5	8.2	56.4	55.1	0.1	0.0	5.78	5.07	44.9	46.0	4.17	4.67	0.083	0.079
Mean	30.2	10.8	84.9	89.6	0.5	0.2	7.81	7.13	45.2	45.4	3.93	5.00	0.127	0.133

References

Allen, R.G., Tasumi, M., 2005. Evaporation from American Falls reservoir in Idaho via a combination of Bowen ratio and eddy covariance, in: Proceedings of the 2005 EWRI Conference, Anchorage, AK. pp. 1–17.

Alpert, P., Shafir, H., Issahary, D., 1997. Recent changes in the climate at the Dead Sea – a preliminary study. Clim. Change 37, 513–537.

Anati, D.A., 1997. The hydrography of a hypersaline lake. In: Niemi, T.M., Ben-Avraham, Z., Gat, J.R. (Eds.), The Dead Sea - the Lake and Its Setting. Oxford University Press, Oxford, pp. 89–103.

Arnon, A., Lensky, N.G., Selker, J.S., 2014. High-resolution temperature sensing in the Dead Sea using fiber optics. Water Resour. Res. 50, 1756–1772. http://dx.doi.org/10.1002/2013WR014935.

Arnon, A., Selker, J.S., Lensky, N.G., 2016. Thermohaline stratification and double diffusion diapycnal fluxes in the hypersaline Dead Sea. Limnol. Oceanogr. 61, 1214–1231. http://dx.doi.org/10.1002/lno.10285.

Assouline, S., 1993. Estimation of lake hydrologic budget terms using the simultaneous solution of water, heat, and salt balances and a Kalman filtering approach: application to Lake Kinneret. Water Resour. Res. 29, 3041–3048. http://dx.doi.org/10.1029/93WR01181.

Assouline, S., Mahrer, Y., 1993. Evaporation from Lake Kinneret: 1. Eddy correlation system measurements and energy budget estimates. Water Resour. Res. 29, 901–910. http://dx.doi.org/10.1029/92WR02432.

Assouline, S., Tyler, S.W., Tanny, J., Cohen, S., Bou-Zeid, E., Parlange, M.B., Katul, G.G., 2008. Evaporation from three water bodies of different sizes and climates: Measurements and scaling analysis. Adv. Water Resour. 31, 160–172. http://dx.doi.org/10.1016/j.advwatres.2007.07.003.

Barenburg, A.W.T., 1974. Psychrometry and Psychrometric Charts. Chamber of Mines, Johannesburg, South Africa.

Brutsaert, W., 2005. Hydrology: An Introduction. Cambridge University Press, Cambridge.

Brutsaert, W., 1982. In: Evaporation into the atmosphere: Theory, history, and applications. D. Riedel Publishing Company. http://dx.doi.org/10.1007/978-94-017-1497-6.

Dalton, J., 1802. Experimental essays on the constitution of mixed gases; on the force of steam or vapor from water and other liquids in different temperatures, both in a Torricellian vacuum and in air; on evaporation and on the expansion of gases by heat. Mem. Manchester Liter. Phil. Soc. 5, 535–602.

Deardorff, J.W., 1966. The counter gradient heat flux in the lower atmosphere and in the laboratory. J. Atmos. Sci. 3, 503–506.

Gertman, I., Hecht, A., 2002. The Dead Sea hydrography from 1992 to 2000. J. Mar. Syst. 35, 169–181. http://dx.doi.org/10.1016/S0924-7963(02)00079-9.

Harbeck, G.E., 1958. Water-loss investigations: Lake Mead studies. US Government Printing Office.

Hect, A., Gertman, I., 2003. Dead Sea Meteorological Climate. Fungal Life Dead Sea 68–114.

Itier, B., Brunet, Y., 1996. Recent developments and present trends in evaporation research: a partial survey, in: Camp, C.R., Sadler, E.J., Yoder, R.E. (Eds.), Evapotranspiration and Irrigation Scheduling, Proceedings of the International Conference ASA. pp. 1–20.

Lensky, I.M., Dayan, U., 2015. Satellite observations of land surface temperature patterns induced by synoptic circulation. Int. J. Climatol. 35, 189–195.

Lensky, I.M., Dayan, U., 2012. Continuous detection and characterization of the Sea Breeze in clear sky conditions using Meteosat Second Generation. Atmos. Chem. Phys. 12, 6505–6513. http://dx.doi.org/10.5194/acp-12-6505-2012.

Lensky, N.G., Dente, E., 2017. The causes for the accelerated rate of Dead Sea level decline in the past decades. Ecol. Environ. 8, 328–336.

Lensky, N.G., Dvorkin, Y., Lyakhovsky, V., Gertman, I., Gavrieli, I., 2005. Water, salt, and energy balances of the Dead Sea. Water Resour. Res. 41, 1–13. http://dx.doi.org/10.1029/2005WR004084.

Lensky, N.G., Lensky, I.M., Peretz, A., Gertman, I., Tanny, J., Assouline, S., 2018. Diurnal course of evaporation from the dead sea in summer: a distinct double peak induced by solar radiation and night sea breeze. Water Resour. Res. 54, 150–160. http://dx.doi.org/10.1002/2017WR021536.

Levy, I., Dayan, U., Mahrer, Y., 2010. Differing atmospheric scales of motion and their impact on air pollutants. Int. J. Climatol. 30, 612–619.

Liu, H., Zhang, Q., Dowler, G., 2012. Environmental controls on the surface energy budget over a large southern inland water in the United States: an analysis of one-year eddy covariance flux data. J. Hydrometeorol. 13, 1893–1910. http://dx.doi.org/10.1175/JHM-D-12-020.1.

Liu, H., Zhang, Y., Liu, S., Jiang, H., Sheng, L., 2009. Eddy covariance measurements of surface energy budget and evaporation in a cool season over southern open water in Mississippi. J. Geophys. Res. 114, D04110. http://dx.doi.org/10.1029/2008JD010891.

MacKellar, M., McGowan, H., 2010. Air-sea energy exchanges measured by eddy covariance during a localised coral bleaching event, Heron Reef, Great Barrier Reef, Australia. Geophys. Res. Lett. 37. http://dx.doi.org/10.1029/2010GL045291.

McGowan, H., Sturman, A., 2010. Measurements of the local energy balance over a coral reef flat, Heron Island, southern Great Barrier Reef, Australia. J. Geophys. Res. Atm.

115, D19124. http://dx.doi.org/10.1029/2010JD014218.
Metzger, J., Nied, M., Corsmeier, U., Kleffmann, J., Kottmeier, C., 2018. Dead Sea evaporation by eddy covariance measurements vs. aerodynamic, energy budget, Priestley-Taylor, and Penman estimates. Hydrol. Earth Syst. Sci. 22, 1135–1155. http://dx.doi.org/10.5194/hess-22-1135-2018.
Mor, Z., Assouline, S., Tanny, J., Lensky, I.M., Lensky, N.G., 2018. Effect of water surface salinity on evaporation: the case of a diluted buoyant plume over the dead sea. Water Resour. Res. 54, 1460–1475. http://dx.doi.org/10.1002/2017WR021995.
Nehorai, R., Lensky, I.M., Hochman, L., Gertman, I., Brenner, S., Muskin, A., Lensky, N.G., 2013a. Satellite observations of turbidity in the Dead Sea. J. Geophys. Res. Ocean. 118, 3146–3160. http://dx.doi.org/10.1002/jgrc.20204.
Nehorai, R., Lensky, I.M., Lensky, N.G., Shiff, S., 2009. Remote sensing of the Dead Sea surface temperature. J. Geophys. Res. C Ocean 114, 4–11 https://doi.org/ArtnC05021/rDoi 10.1029/2008jc005196.
Nehorai, R., Lensky, N.G., Brenner, S., Lensky, I.M., 2013b. The dynamics of the skin temperature of the dead sea. Adv. Meteorol. 2013. http://dx.doi.org/10.1155/2013/296714.
Sade, A., Hall, J.K., Sade, H., Amit, G., Tibor, G., Schulze, B., Gur-Arieh, L., Ten Brink, U., Ben-Avraham, Z., Keller, C., 2014. Multibeam bathymetric map of the Dead Sea. Geol. Surv. Isr. Rep GSI/01/2014.
Salameh, E., El-Naser, H., 1999. Does the actual drop in Dead Sea level reflect the development of water sources within its drainage basin? Acta Hydrochim. Hydrobiol. 27, 5–11. http://dx.doi.org/10.1002/(SICI)1521-401X(199901)27:1<5::AID-AHEH5>3.0.CO;2-Z.
Salhotra, A.M., Adams, E.E., Harleman, D.R.F., 1985. Effect of Salinity and Ionic Composition on Evaporation: Analysis of the Dead Sea Evaporation Pans. Water Resour. Res. 21, 1336–1344. http://dx.doi.org/10.1029/WR021i009p01336.
Sirota, I., Arnon, A., Lensky, N.G., 2016. Seasonal variations of halite saturation in the Dead Sea. Water Resour. Res. 52. http://dx.doi.org/10.1002/2016WR018974.
Sirota, I., Enzel, Y., Lensky, N.G., 2017. Temperature seasonality control on modern halite layers in the Dead Sea: In situ observations. Geol. Soc. Am. Bull. B31661–B31671.
Stanhill, G., 1994. Changes in the rate of evaporation from the Dead Sea. Int. J. Clim. 14, 465–471.
Stannard, D.I., Rosenberry, D.O., 1991. A comparison of short-term measurements of lake e vaporation using eddy correlation and energy budget methods. J. Hydrol. 122, 15–22.
Steinhorn, I., 1983. In situ salt precipitation at the Dead Sea. Limnol. Oceanogr. 28, 580–583.
Steinhorn, I., 1981. A hydrographical and physical study of the Dead Sea during destruction of its long-term meromictic stratification. Feinb. Grad. Sch. Weizmann Inst. of Sci, Rehovot.
Steinhorn, I., Assaf, G., 1980. The Physical Structure of the Dead Sea Water Column–1975–1977. Dev. Sedimentol. 28, 145–153.
Stiller, M., Gat, J.R., Kaushansky, P., 1997. Halite precipitation and sediment deposition as measured in sediment traps deployed in the Dead Sea: 1981–1983. OXFORD Monogr. Geol. Geophys. 36, 171–183.
Tanny, J., Cohen, S., Assouline, S., Lange, F., Grava, A., Berger, D., Teltch, B., Parlange, M.B.B., 2008. Evaporation from a small water reservoir: Direct measurements and estimates. J. Hydrol. 351, 218–229. http://dx.doi.org/10.1016/j.jhydrol.2007.12.012.
Tanny, J., Cohen, S., Berger, D., Teltch, B., Mekhmandarov, Y., Bahar, M., Katul, G.G., Assouline, S., 2011. Evaporation from a reservoir with fluctuating water level: correcting for limited fetch. J. Hydrol. 404, 146–156.